J Mater Sci: Mater Electron (2025) 36:40

Analysis of Nb-doped and undoped TiO_2 nanocoatings with varying dopant concentrations

Öznur Arslan[1,2], Halil İbrahim Efkere[3], Erman Çokduygulular[4], Çağlar Çetinkaya[2], Caner İldeş[5], and Barış Kınacı[3,6,*]

[1] *Institute of Graduate Studies in Sciences, Istanbul University, 34116 Istanbul, Turkey*
[2] *Physics Department, Faculty of Science, Istanbul University, 34134 Istanbul, Turkey*
[3] *Photonics Application and Research Center, Gazi University, 06500 Ankara, Turkey*
[4] *Department of Engineering Sciences, Faculty of Engineering, Istanbul University-Cerrahpaşa, 34320 Istanbul, Turkey*
[5] *Application and Research Center of Science and Technology, Yozgat Bozok University, 66900 Yozgat, Turkey*
[6] *Department of Photonics, Faculty of Applied Sciences, Gazi University, 06500 Ankara, Turkey*

Received: 1 October 2024
Accepted: 12 December 2024

© The Author(s), under exclusive licence to Springer Science+Business Media, LLC, part of Springer Nature, 2024

ABSTRACT

Titanium dioxide (TiO_2) without doped and with different amounts of niobium (Nb) doped coating with thicknesses of ~ 100 nm were deposited on glass and n-Si substrates at room temperature by radio frequency magnetron sputtering. Nb doping ratios were determined as 0% (NTO-0), 3% (NTO-3), 5% (NTO-5), and 7% (NTO-7). Structural, morphological, and optical analyses of NTO-0, NTO-3, NTO-5, and NTO-7 samples on a glass substrate were performed. The X-Ray Diffraction method performed the structures' crystallite quality. Quantitative elemental microanalysis of the structure was performed by scanning electron microscopy with the energy dispersive spectroscopy method. The surface morphologies of the structures were performed by the Atomic Force Microscope system. The transmittance spectra of the structures were performed by UV–Visible Spectrometer systems. The electrical properties of the Au/n-Si structure with TiO_2 interface layer doped 3% Nb depending on the frequency (between 100 kHz to 1 MHz) and the voltage (in the range of ± 4 V) using *C–V* and *G/ω–V* characteristics were obtained.

1 Introduction

Titanium dioxide (TiO_2) films are used in a wide range of applications in various fields, such as solar cells, photocatalysis, gas sensing, optoelectronics, etc. [1–4]. TiO_2 is a widely studied semiconductor material known for its high refractive index, optical transparency, and chemical stability. TiO_2, one of the vital parts in perovskite solar devices, separates excitons and delivers electrons to the conductive substrate [5, 6]. There are three different phases in pure titanium dioxide polymorphs: rutile, anatase, and brookite phases [7]. However, only anatase and rutile structures are observed in thin film form [8]. In addition to these crystalline phases, an amorphous TiO_2 structure is observed when the substrate temperature is very low during deposition [9].

Address correspondence to E-mail: bariskinaci@gazi.edu.tr

https://doi.org/10.1007/s10854-024-14092-0
Published online: 24 December 2024

Doping is a process that involves adding small amounts of foreign atoms (dopants) to the TiO_2 lattice. This process is done to change the electronic, optical, and structural properties of TiO_2 and improve its performance in certain applications [10]. Pure TiO_2 has a wide bandgap, making it responsive primarily to UV light. Doping can reduce the bandgap, enabling visible light absorption and enhancing photocatalytic activity [11–13]. Doping can introduce new energy levels within the bandgap, improving charge carrier mobility, reducing recombination rates, and thereby enhancing the material's conductivity. Commonly used dopants can be given as: Non-metal Dopants: Elements like nitrogen (N) [14], carbon (C) [15], and sulfur (S) [16] are commonly used to introduce states within the bandgap, making TiO_2 responsive to visible light. Metal Dopants: Transition metals like iron (Fe) [17], chromium (Cr) [18], vanadium (V) [19], and niobium (Nb) [20] are often used to introduce localized states that improve the photocatalytic efficiency under visible light. Noble metals like gold (Au) and silver (Ag) [21] can also be used to enhance plasmonic effects. Rare Earth Elements: Elements like lanthanum (La), cerium (Ce) [22], and europium (Eu) [11] are sometimes doped into TiO_2 to enhance luminescence properties or modify the electronic structure. Numerous doping materials have been explored for TiO_2, with Nb doping standing out as a strategy to promote defect state formation and enhance the surface activity of TiO_2 films, facilitating redox reactions. This approach aims to achieve simultaneous improvements in both electrochemical and optical performance [23]. While doping can significantly improve the properties of TiO_2, it can also introduce defects that may lead to increased recombination centers, reducing photocatalytic efficiency. Therefore, optimizing the type and concentration of dopants is critical for achieving the desired properties without compromising the material's overall performance. Doped TiO_2 thin films represent a versatile and promising material with wide-ranging technological applications, particularly as researchers continue exploring new doping strategies to tailor their properties for specific needs.

TiO2 thin films can be prepared by many different methods, such as sol–gel [24], pulsed laser deposition [25], chemical vapor deposition (CVD), spray pyrolysis [26], spin coating [27] and RF magnetron sputtering [28] techniques. Among these systems, the sol–gel method has a lower cost than others. Among these methods, RF magnetron sputtering stands out with its ability to produce thin films of good quality, good adhesion, high transparency, and uniform thickness [29]. Magnetron sputtering of TiO_2 films is also attracting attention as it is a feasible industrial process for large-area deposition [30]. Additionally, controllable deposition parameters and low substrate temperature are among the advantages that should be mentioned [29].

In the current study, the TiO_2 structure was doped with the niobium (Nb) element, which is among the transition metals, and its analysis was focused on undoped, and 3, 5, and 7% Nb-doped TiO_2 layers were deposited onto glass and silicon substrates in an RF magnetron sputtering system. Undoped TiO_2, 3% Nb-doped TiO_2, 5% Nb-doped TiO_2, and 7% Nb-doped TiO_2 thin films are referred to as NOT–0, NTO-3, NTO-5, and NTO-7, respectively. The crystalline phases of all films were investigated using XRD analysis. Quantitative elemental microanalysis was conducted using the SEM–EDS method for NTO-0 and NTO-3 structures to confirm the chemical composition and elemental content of the synthesized nanocoatings. All films' surface morphology and transmittance spectra were reported using AFM and UV–Vis measurements. According to the results obtained, changing the Nb ratio affected the structural, morphological, optical, and electrical properties of TiO_2 films. Therefore, the capacitance–voltage and conductance-voltage characteristics of the NTO-3 structure were investigated in a wide frequency range of 100 kHz to 1 MHz at ± 4 V.

2 Material and methods

In this study, undoped TiO_2 and TiO_2 thin films doped with different ratios of Niobium (Nb) were produced on n-Si and glass substrates using the RF magnetron sputtering technique. The Si substrate utilized in this study is phosphorus-doped, with a thickness of 380 μm, a resistivity ranging from 1 to 10 Ω·cm, and a double-sided polished surface. Prior to coating, n-Si substrates were cleaned in an ultrasonic bath for 5 min each with acetone and isopropyl alcohol, respectively. Glass substrates were washed with detergent and sponge to remove organic and inorganic contaminants from the surface and rinsed with deionized water (DI–Water). All n-Si and glass substrates completed with cleaning and rinsing processes were dried with high-purity dry nitrogen gas and loaded into the co–sputtering (Nanovak NVTS–500)

deposition system. The co–sputtering system was pumped down until it reached a base vacuum level of 10^{-7} Torr. The distance between each of the TiO_2 and Nb (99.9% pure and 2–inch dia., each) targets used in the processes and the sample holder was set to 10 cm. The deposition processes for undoped and Nb-doped TiO_2 were conducted at room temperature. The parameters utilized in all processes, including coating pressure, power, and substrate rotation speed, were maintained at 10 mTorr, 120 W (for both undoped and Nb-doped TiO_2), and 5 rpm, respectively. The power values applied to the Nb target in the doped TiO_2 processes are 4, 6, and 8 W, respectively. With the completion of the depositions, undoped TiO_2, 3% Nb-doped TiO_2, 5% Nb-doped TiO_2, and 7% Nb-doped TiO_2 thin films were obtained, and these samples are referred to as NTO-0, NTO-3, NTO-5, and NTO-7, respectively. The thicknesses of each sample set obtained were measured as ~ 100 nm with a Veeco Dektak 150 Stylus Tip Profilometer. Elemental analysis of Nb-doped and undoped structures were analyzed using an FEI Quanta FEG 450 model SEM device equipped with an EDS analyzer. The entire nanocoatings were structurally characterized by XRD spectroscopy in the diffraction angle range of $20° \leq 2\theta \leq 60°$ in steps of 0.01° using a Bruker Advance D8 XRD diffractometer. Nanomagnetics Atomic Force Microscope (AFM) system was used for morphological analysis of all undoped and Nb-doped TiO_2 thin films obtained at different ratios, and Lambda 2S UV–Visible Spectrometer (UV–Vis) systems were used for the characterization of optical properties of thin films deposited on glass.

In order to perform capacitance–voltage (C–V) and conductance/angular frequency–voltage (G/ω–V) analysis of NTO-3, a 150 nm thick Au (99.9% pure) metal contact was made to the back surface of the n-Si sample in a thermal evaporation system. The back contact was ohmicized by annealing the sample in a Rapid Thermal Annealing (RTA) system at 350 °C for 3 min in a vacuum environment. Then, again with the thermal evaporation system, Au front Schottky contacts were taken at room temperature with a thickness of 150 nm using a shadow circular (1 mm dia.) mask.

C–V and G/ω–V measurements were conducted on the fabricated Au/Nb-doped TiO_2/n-Si/Au structure. These measurements were performed at room temperature by applying a 50 mV AC signal across a frequency range of 100 kHz to 1 MHz. An HP 4192A LF impedance analyzer was utilized in conjunction with the measurement systems for both the C–V and G/ω–V analyses.

3 Results and discussion

Nb-doped TiO_2 (NTO) nano–coated films with varying Nb doping concentrations were prepared using sputter technology. The prepared films (niobium atomic percentages: 0%, 3%, 5%, and 7%) were labeled as NTO-0, NTO-3, NTO-5, and NTO-7, respectively. To confirm the synthesized nanocoatings' chemical composition and elemental content, quantitative elemental microanalysis was conducted using the SEM–EDS method for structures without Nb doping (NTO-0) and with 3% Nb doping (NTO-3). The EDS analysis of the NTO-0 structure revealed an elemental map, presented in Fig. 1a, which clearly shows distinct peaks corresponding to the presence of O and Ti. Additionally, the inset in Fig. 1 displays a surface SEM image of the NTO-0 structure with a scanning area of 500 nm, providing insights into its surface morphology. Similarly, the EDS analysis of the NTO-3 structure yielded an elemental map, shown in Fig. 1b, where peaks corresponding to Nb, O, and Ti are evident. The Nb content was quantified as 2.73%, aligning closely with the intended doping concentration of 3%. The inset in Fig. 1b includes a surface SEM image of the NTO-3 structure, also scanned over a 500 nm area, offering additional details about its surface morphology.

The crystalline phases of all films were investigated by XRD analysis, as shown in Fig. 2. From Fig. 2a, all the diffraction peaks of the films were identified as pure anatase TiO_2 phase with tetragonal structure (JCPDS 71-1166). The diffraction peaks belong to the (101), (004), (103), and (200) planes of anatase TiO_2, respectively, which is consistent with the tetragonal structured TiO_2. No other peaks are found for NTO-3, NTO-5, and NTO-7 films, which means that Nb doping does not change the crystal structure of TiO_2 films. Moreover, by examining Fig. 2(b), the diffraction peaks become increasingly broader and weaker with the increase of Nb doping content, indicating that the crystallinity and grain size of TiO_2 films decreases.

Surface roughness plays a crucial role in determining material performance in optoelectronic applications, including photocatalysis, sensors, and solar cells. Given that doping can significantly influence the surface energy and roughness of TiO_2 [21], conducting a detailed morphological characterization of

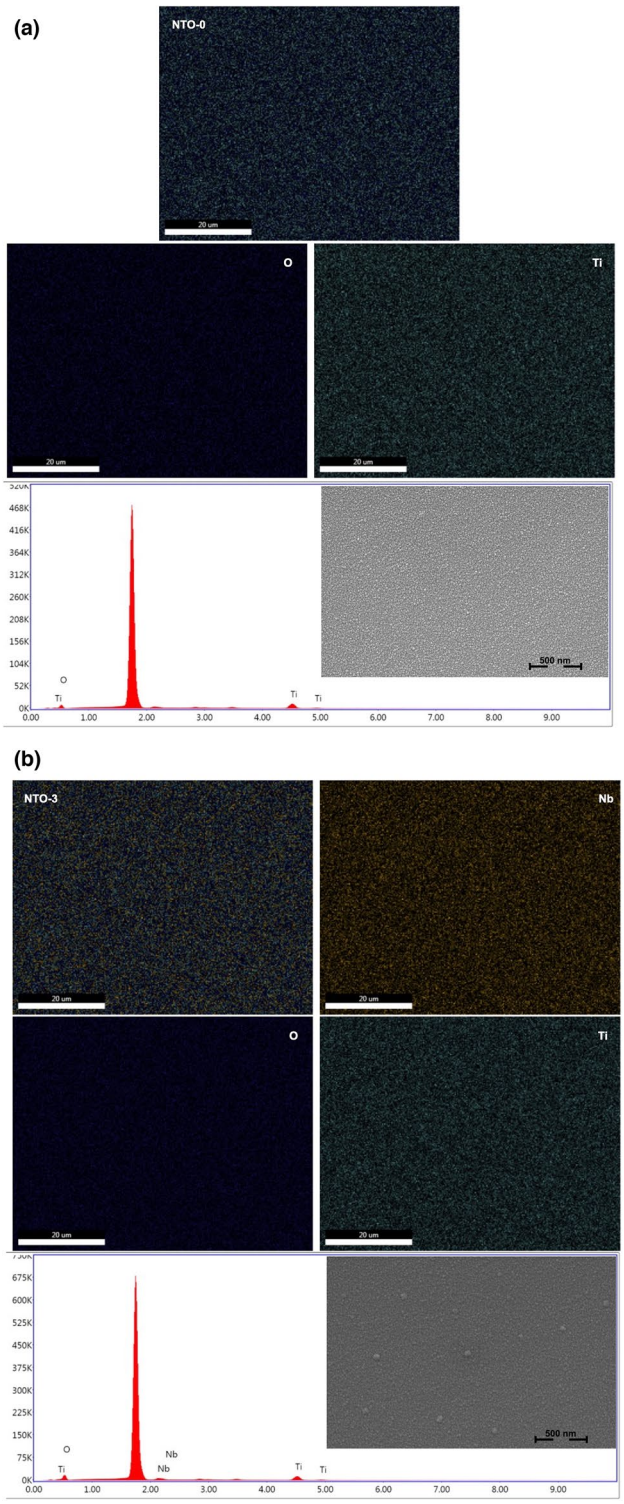


Fig. 1 **a** Summary of SEM–EDS analysis results of NTO-0 structure. **b** Summary of SEM–EDS analysis results of NTO-3 structure

doped TiO_2 is essential for optimizing its performance. The surface morphology and roughness affecting the physical behavior of samples NTO-0, NTO-3, NTO-5, and NTO-7 were evaluated using AFM measurements. Figure 3a–d shows the two-dimensional (2D), and Fig. 4a–d shows the three-dimensional (3D) surface morphologies of nanocoatings deposited on a glass substrate for a 3×3 μm^2 scan area. The surface morphology of the NTO-0 structure changed with the doping ratio, and the lowest root mean square (RMS) roughness was obtained from the NTO-3 structure. The RMS roughness of the samples is listed in Table 1. It is observed that the RMS roughness of samples NTO-0, NTO-3, NTO-5, and NTO-7 are in the range of 0.88 to 1.03 nm (Table 1). As can be seen from the XRD peaks given in Fig. 1a, changes in the surface morphology of TiO_2 thin films were observed due to the change in crystallinity and grain size of TiO_2 films due to doping.

Doping directly influences the optical band gap of TiO_2 by altering its band structure, defect density, and bonding states. The extent of this effect depends on the type and concentration of the dopant as well as the doping method employed. As dopants, metal ions or metal oxides can modify the optical band gap of TiO_2, resulting in either a narrowing or widening of the band gap [31, 32]. Therefore, comprehensive optical characterization of doped TiO_2 is crucial for optimizing its performance. The optical transmittance (T) spectra of the samples NTO-0, NTO-3, NTO-5, and NTO-7 were recorded using a UV–Vis spectrometer in the wavelength range of 200–1100 nm. Figure 5a–d shows the transmittance spectra of these samples' nanocoatings on the glass. Each image has $(\alpha h\nu)^{2-}$ photon energy ($h\nu$) plots, estimating the optical band gap values of 100 nm thick deposited NTO-0, NTO-3, NTO-5, and NTO-7 structures. The values were determined by extrapolating the curves' straight–line portion to zero absorption coefficient. The absorption coefficient can be extracted using only the strong absorption region in the spectra. In addition, interference effects can be neglected in the prediction of E_g. The E_g values of samples NTO-0, NTO-3, NTO-5, and NTO-7 range from 3.333 to 3.454 eV (Table 1). While the E_g value of the NTO-3 structure is lower than that of the NTO-0 structure, the E_g values of the NTO-5 and NTO-7 structures are higher than that of the NTO-0 structure.

As can be seen from both AFM and UV–Vis results, the NTO-3 structure exhibited decreased RMS and E_g values compared to the other samples. This result is

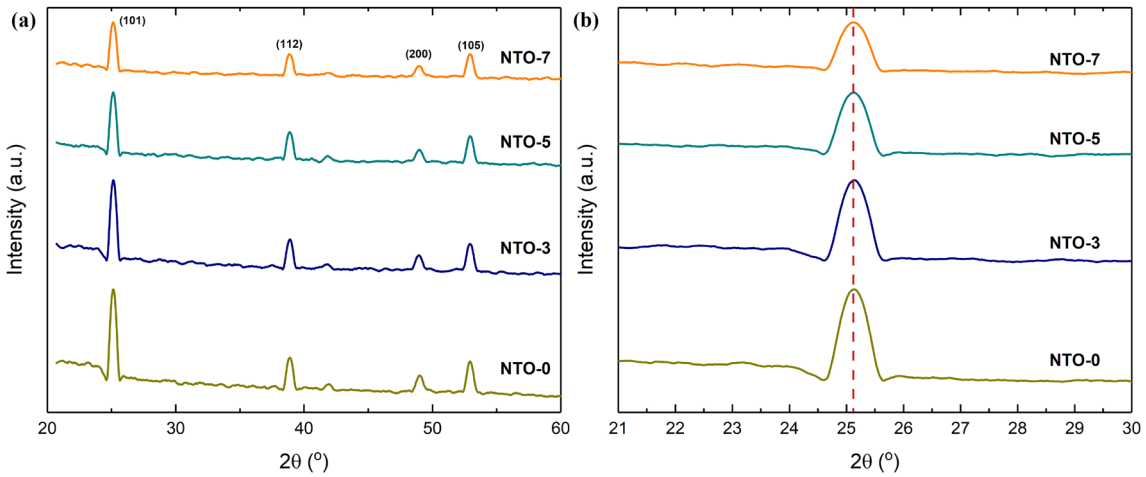


Fig. 2 **a** XRD patterns and **b** magnified XRD patterns of NTO-0, NTO-3, NTO-5, and NTO-7 nano–coated films

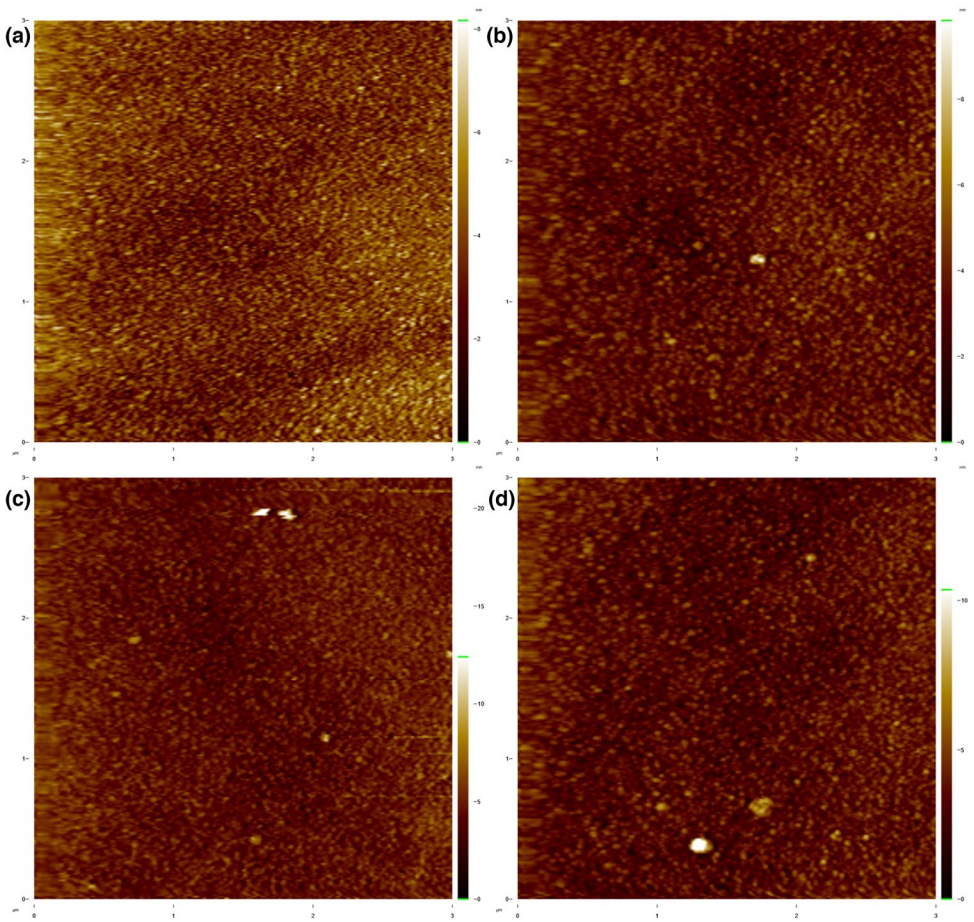


Fig. 3. 2D AFM images; **a** NTO-0, **b** NTO-3, **c** NTO-5, and **d** NTO-7

interesting and motivated us to examine the capacitance and conductance characterization of the sample. The capacitance and conductance characterization of doped TiO_2 structure is very important to understand the electrical properties of the material. These properties depend on factors such as the dielectric constant

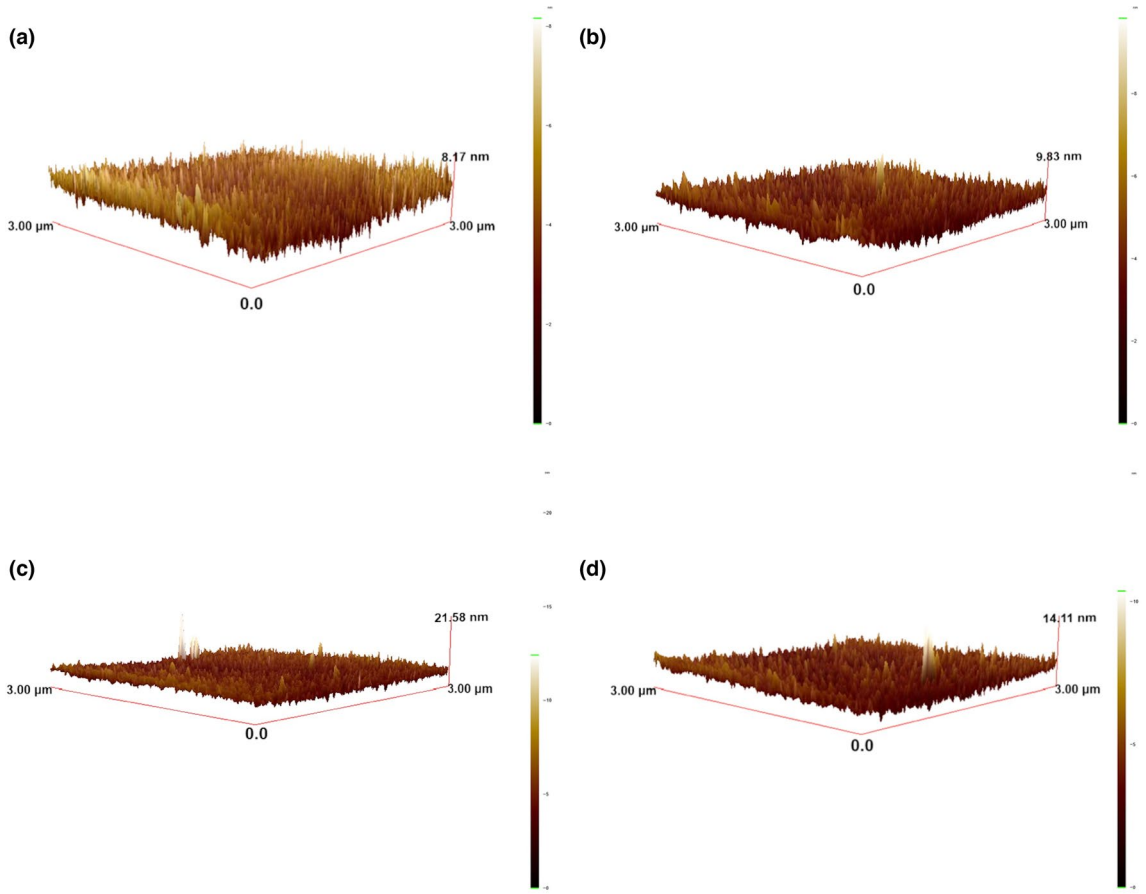


Fig. 4. 3D AFM images; **a** NTO-0, **b** NTO-3, **c** NTO-5, and **d** NTO-7

Table 1 AFM and UV–Vis spectrometer spectrometer parameters of the samples

Sample	RMS roughness (nm)	E_g (eV)
NTO-0	0.98	3.406
NTO-3	0.88	3.333
NTO-5	1.03	3.416
NTO-7	0.98	3.454

of TiO_2, its charge transport ability, and electron–hole (charge carrier) dynamics. Dopants can change the properties of TiO_2 and affect the material's performance in various electronic and optoelectronic applications [33–36]. Capacitance refers to the ability of a material to store electrical charge. In dielectric materials such as TiO_2, capacitance values depend on the dielectric constant, thickness, and surface area of the material. Dopants can increase or decrease the dielectric constant of TiO_2, which can increase or decrease the capacitance values. Capacitance can vary with frequency. At lower frequencies, the capacitance of TiO_2 is generally higher because charge carriers move more easily at these frequencies. Doping can affect this frequency dependence and can be used to optimize the material's performance. Additives can affect capacitance values by creating charge accumulation on the surface and interfaces. Especially in thin film structures, surface and interface doping can cause capacitance values to increase or decrease. Conductance (or conductivity) indicates the ability of a material to conduct electric current.

The conductance of doped TiO_2 is directly related to carrier concentration, mobility, and defects created by the dopant in the material. Dopants can increase the free electron or hole carrier density of TiO_2. For example, metal dopants (e.g., Nb, W) can increase the conductance by increasing the density of electron carriers [23, 36]. This is a desirable feature, especially in photocatalytic applications and sensor technologies. Dopants can prevent electron–hole recombination by creating active sites in TiO_2, and thus extend

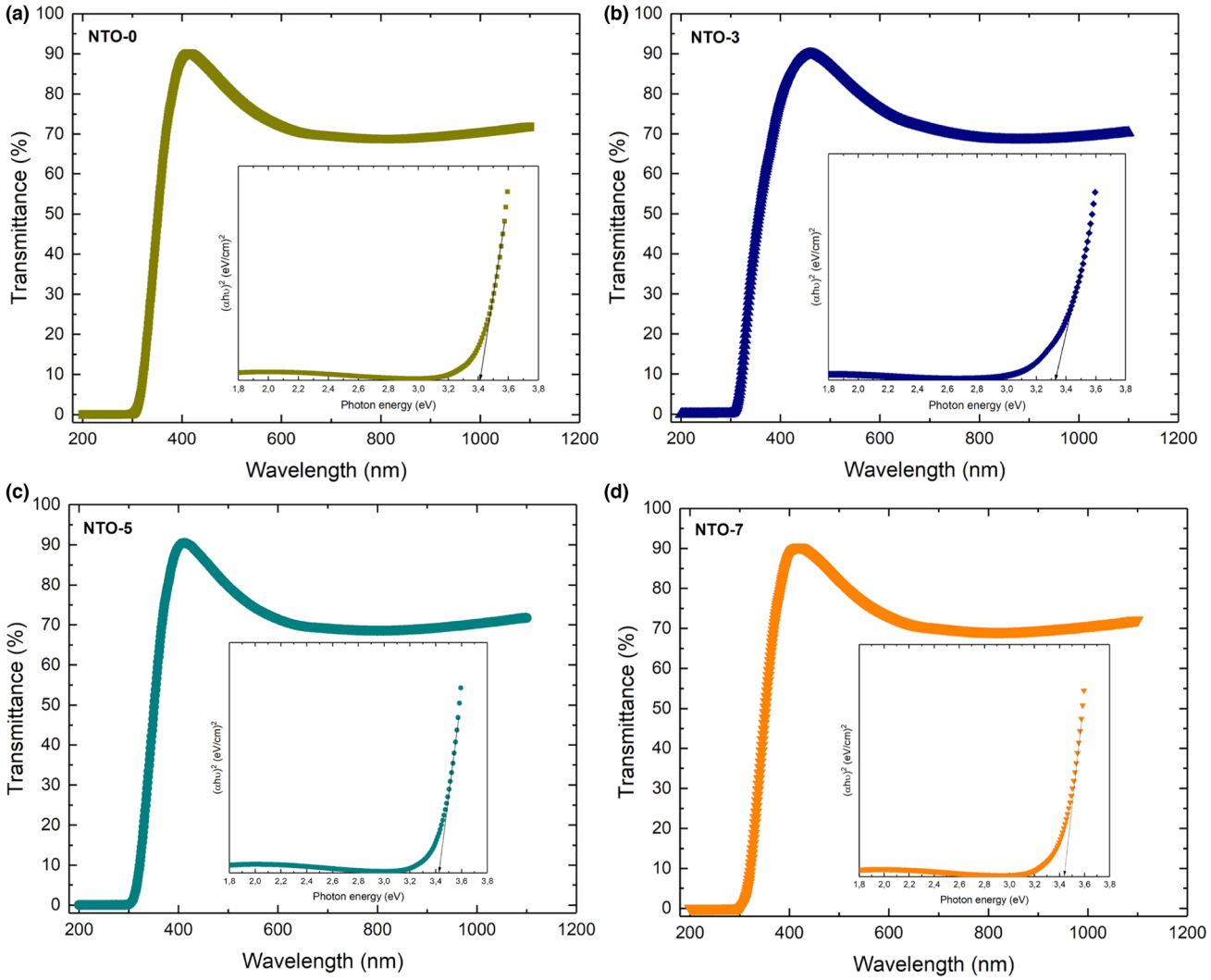


Fig. 5 Transmittance spectra and $(\alpha hv)^2 - hv$ plots (insets); **a** NTO-0, **b** NTO-3, **c** NTO-5, and **d** NTO-7

the carrier lifetime. This can especially affect the frequency dependence of conductance since long–lived carriers provide better conduction at low frequencies. The capacitance and conductance characterization of doped TiO_2 is usually performed by AC impedance spectroscopy. This method helps better understand the material's electrical properties by measuring the capacitance and conductance values that vary with frequency [37–41]. That is, the capacitance and conductance characterization of doped TiO_2 is a critical step in evaluating the electrical performance of the material. Dopants can optimize the capacitance and conductance values by affecting the dielectric constant, charge carrier density, and mobility of TiO_2. These properties are important in determining the effectiveness of TiO_2 in various applications, such as energy storage, sensors, and photocatalysis. Therefore, the capacitance and conductance analysis of the bottom and top contacts of the NTO-3 structure deposited on the silicon substrate (the deposit process was carried out simultaneously with the glass substrate) was investigated in a wide frequency range. The capacitance is highly dependent on the electrical and dielectric properties of the used intermediate layer due to the interface states. In this study, the C–V–f and G/ω–V–f characteristics of the Au/n-Si structure with 3% Nb-doped TiO_2 interface layer in the frequency range of 100 kHz to 1 MHz were obtained, and its electrical properties were investigated in detail.

The C–V–f and G/ω–V–f distributions of the Au/n-Si structure with 3% Nb-doped TiO_2 interface layer are given in Figs. 6a and b, respectively.

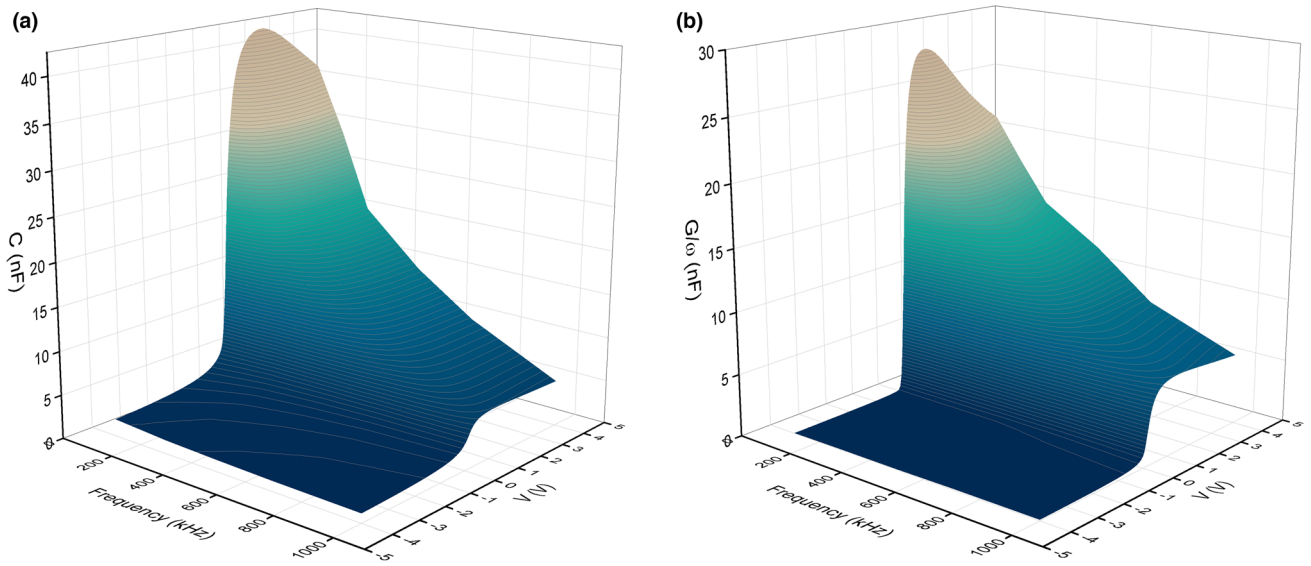


Fig. 6 Frequency–dependent distributions of Au/n-Si structure with 3% Nb-doped TiO_2 interface layer **a** C–V–f, and **b** G/ω–V–f

To achieve more reliable and accurate results, C and G/ω measurements were conducted at room temperature within the ± 4 V range and across a broad frequency spectrum. As can be observed from both figures, the C and G/ω values exhibit significant frequency–dependent variations, encompassing regions of accumulation, depletion, and inversion. Since surface states can easily follow an external alternating current (AC) signal at low frequencies, particularly in the depletion and accumulation regions, changes in both C and G/ω are more pronounced. Additionally, the C and G/ω values observed at high frequencies are lower than those observed at low frequencies due to parameters such as interface states, series resistance, and relaxation times, which must be taken into account to ensure the accuracy and reliability of electrical measurements [42]. Series resistance (R_s) is regarded as one of the key parameters influencing the non-ideal electrical behavior of the structure. Various methods have been proposed in the literature for determining R_s, and in this study, the method developed by Nicollian and Brews was utilized [43, 44].

$$R_s = \frac{G_m}{G_m^2 + \left(\omega C_m\right)^2} \tag{1}$$

In this approach, C_m and G_m represent the capacitance and conductance measured at a given bias voltage.

The R_s values were calculated using Eq. (1) and are presented in Fig. 7 for different frequencies.

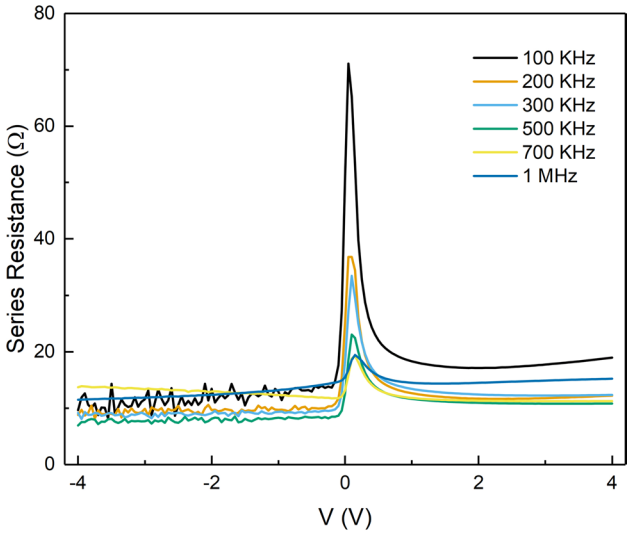


Fig. 7 R_s versus V for Au/n-Si structure with 3% Nb-doped TiO_2 interface layer

Specifically, these values were determined for all frequency values and summarized in Table 1. As illustrated in Fig. 7, the R_s values do not exhibit a linear relationship with frequency. The minimum R_s value was observed at a frequency of 500 kHz.

Equation 2 describes the relationship between the reverse bias voltage (V_R) and the capacitance per unit area [45].

$$C^{-2} = \frac{2(V_0 + V_R)}{q\epsilon_s\epsilon_0 A^2 N_D} \tag{2}$$

Table 2 Some electrical parameters obtained for all frequency values

Frequency (kHz)	V_0 (V)	V_D (eV)	Φ_B (eV)	R_s (at 4 V) (Ω)
100	0,571	0,597	0.670	18.990
200	0,556	0,581	0.665	12.254
300	0,600	0,626	0.717	12.380
500	0,800	0,826	0.913	10.845
700	0,500	0,526	0.642	11.270
1000	0,500	0,526	0.642	15.254

In this equation, V_0 and N_D correspond to the intercept and slope of the C^{-2} versus V curve, respectively. From these parameters, fundamental electronic properties of the Au/n-Si structure with 3% Nb-doped TiO_2 interface layer structure, such as the diffusion potential (V_D) and barrier height (Φ_B ($C-V$)), were determined for all frequency values and summarized in Table 2 [46–51].

$$V_D = V_0 + \frac{kT}{q} \tag{3}$$

$$\Phi_B = V_D + E_F + \Delta\Phi_B \tag{4}$$

4 Conclusions

NTO-0, NTO-3, NTO-5, and NTO-7 structures were deposited as coatings with thicknesses of approximately 100 nm on glass and n-Si substrates at room temperature using radio frequency (RF) magnetron sputtering. The nanocoatings' chemical composition and elemental content were analyzed using SEM–EDS for undoped (NTO-0) and 3% Nb-doped (NTO-3) structures on an n-Si substrate. EDS results for NTO-3 confirmed the presence of Nb, O, and Ti, with Nb content quantified at 2.73%, closely matching the target doping level. Structural, morphological, and optical characterizations of the NTO-0, NTO-3, NTO-5, and NTO-7 structures deposited on glass substrate were carried out using XRD, AFM, and UV–Vis systems, respectively. XRD analysis revealed that all films exhibit a pure anatase TiO_2 phase with a tetragonal structure, with diffraction peaks corresponding to the (101), (004), (103), and (200) planes. Increasing Nb doping content does not alter the crystal structure but leads to broader and weaker (101) peaks, indicating reduced crystallinity and grain size.

Morphological and optical characterizations of the samples deposited on glass substrate were carried out using AFM and UV–Vis systems, respectively. 2D and 3D surface morphologies obtained from AFM analyses were used to evaluate the surface morphology and roughness of samples NTO-0, NTO-3, NTO-5, and NTO-7. However, it is unclear how the doping rate affects the surface changes, especially considering that the lowest RMS roughness was obtained from the NTO-3. The E_g values of the samples, ranging from 3.333 to 3.454 eV, indicate that while the NTO-3 structure exhibits a lower E_g compared to NTO-0, NTO-5, and NTO-7 structures show higher E_g values, likely due to the diffusion of titanium, niobium, and oxygen into the TiO_2 lattice, where oxygen vacancies and interstitials influence the energy bandgap. In addition, when the RMS values obtained from AFM are taken into account, the lowest E_g value (3.333 eV) obtained from the NTO-3 shows that the results are consistent and related to each other. Additionally, the frequency-dependent (between 100 kHz to 1 MHz) capacitance and conductance analyses of the NTO-3 structure were investigated in detail. Frequency-dependent analysis revealed that both C–V and G/ω–V characteristics exhibited accumulation, depletion, and inversion regions, with the values of both C and G/ω being strongly dependent on frequency. It was also observed that the C and G/ω values decreased with increasing frequency due to interface states, series resistance, and relaxation times within the structure. Notably, the capacitance (C) showed a sharper change at lower frequencies compared to G/ω, as surface states can more easily follow an external alternating current signal. In contrast, the change in G/ω at low frequencies was less pronounced, influenced by fundamental parameters such as interface traps, relaxation times, and their reorganization under an external electric field. Furthermore, R_s, one of the critical parameters for device performance, was calculated for each frequency. At a bias voltage of 4 V, the lowest R_s value was determined to be 10.845 (Ω) at a frequency of 500 kHz. As a result, it was observed that the NTO-3 is quite suitable for applications such as interface layer, electron transport layer, etc., for an optoelectronic device application due to its low surface roughness, band gap shift, and ideal capacitance and conductance behaviors.

Acknowledgements

This study was supported by the Directorate of the Presidential Strategy and Budget of Turkey (Project No: 2019K12-149045).

Author contributions

Öznur Arslan: Investigation, Visualization, Formal Analysis. Halil İbrahim Efkere: Conceptualization, Investigation. Erman Çokduygulular: Formal analysis and Visualization. Çağlar Çetinkaya: Conceptualization, Formal analysis. Caner İldeş: Investigation, Visualization. Barış Kınacı: Writing – review and editing, and Supervision.

Funding

The funders had no role in the study design, data collection and analysis, decision to publish, or manuscript preparation.

Data availability

The data supporting the findings of this study are available upon reasonable request from the authors.

Declarations

Conflict of interest There are no conflict to declare.

References

1. K.H. Ko, Y.C. Lee, Y.J. Jung, J. Colloid Interface Sci. **283**, 482 (2005)
2. J. Yu, X. Zhao, Q. Zhao, Mater. Chem. Phys. **69**, 25 (2001)
3. B. Karunagaran, P. Uthirakumar, S.J. Chung, S. Velumani, E.-K. Suh, Mater Charact **58**, 680 (2007)
4. S. Nezar, N. Saoula, S. Sali, M. Faiz, M. Mekki, N.A. Laoufi, N. Tabet, Appl. Surf. Sci. **395**, 172 (2017)
5. I.J. Kramer, J.C. Minor, G. Moreno-Bautista, L. Rollny, P. Kanjanaboos, D. Kopilovic, S.M. Thon, G.H. Carey, K.W. Chou, D. Zhitomirsky, A. Amassian, E.H. Sargent, Adv. Mater. **27**, 116 (2015)
6. B. Susrutha, L. Giribabu, S.P. Singh, Chem. Commun. **51**, 14696 (2015)
7. A. Golubović, M. Šćepanović, A. Kremenović, S. Aškrabić, V. Berec, Z. Dohčević-Mitrović, Z.V. Popović, J. Sol–Gel Sci. Technol. **49**, 311 (2009)
8. P.B. Nair, V.B. Justinvictor, G.P. Daniel, K. Joy, V. Ramakrishnan, P.V. Thomas, Appl. Surf. Sci. **257**, 10869 (2011)
9. L.M. Williams, D.W. Hess, J. Vacuum Sci. Technol. A: Vacuum Surf. Films **1**, 1810 (1983)
10. K.S. Varma, R.J. Tayade, K.J. Shah, P.A. Joshi, A.D. Shukla, V.G. Gandhi, Water-Energy Nexus **3**, 46 (2020)
11. E. Cerrato, E. Gaggero, P. Calza, M.C. Paganini, Chem. Eng. J. Adv. **10**, 100268 (2022)
12. A. Khlyustova, N. Sirotkin, T. Kusova, A. Kraev, V. Titov, A. Agafonov, Mater. Adv. **1**, 1193 (2020)
13. N.S. Ibrahim, W.L. Leaw, D. Mohamad, S.H. Alias, H. Nur, Int. J. Hydrogen Energy **45**, 28553 (2020)
14. S. Du, J. Lian, F. Zhang, Trans. Tianjin Univ. **28**, 33 (2022)
15. C.-C. Yang, C.-X. Wang, C.-Y. Kuan, C.-Y. Chi, C.-Y. Chen, Y.-Y. Lin, G.-S. Chen, C.-H. Hou, F.-H. Lin, Antioxidants **9**, 880 (2020)
16. A. Piątkowska, M. Janus, K. Szymański, S. Mozia, Catalysts **11**, 144 (2021)
17. M. Ismael, J. Environ. Chem. Eng. **8**, 103676 (2020)
18. H.H. Nguyen, G. Gyawali, A. Martinez-Oviedo, Y.K. Kshetri, S.W. Lee, J. Photochem. Photobiol. A Chem. **397**, 112514 (2020)
19. H. Wang, F. Zhang, M. Jin, D. Zhao, X. Fan, Z. Li, Y. Luo, D. Zheng, T. Li, Y. Wang, B. Ying, S. Sun, Q. Liu, X. Liu, X. Sun, Mater. Today Phys. **30**, 100944 (2023)
20. M. Yuasa, Ceram. Int. **48**, 14726 (2022)
21. D. Gogoi, A. Namdeo, A.K. Golder, N.R. Peela, Int. J. Hydrogen Energy **45**, 2729 (2020)
22. K. Wu, M. Debliquy, C. Zhang, Chem. Eng. J. **444**, 136449 (2022)
23. B. Zhang, J. Luo, Z. Chen, Y. Xiang, L. Tang, H. Jiang, Y. Tian, S. Liu, Opt. Mater. (Amst.) **131**, 112728 (2022)
24. C.J. Brinker, M.S. Harrington, Solar Energy Mater. **5**, 159 (1981)
25. J.-H. Kim, S. Lee, H.-S. Im, Appl. Surf. Sci. **151**, 6 (1999)
26. A. Möllmann, D. Gedamu, P. Vivo, R. Frohnhoven, D. Stadler, T. Fischer, I. Ka, M. Steinhorst, R. Nechache, F. Rosei, S.G. Cloutier, T. Kirchartz, S. Mathur, Adv. Eng. Mater. **21**, 1 (2019)
27. I.N. Kuznetsova, V. Blaskov, I. Stambolova, L. Znaidi, A. Kanaev, Mater. Lett. **59**, 3820 (2005)
28. Y.-M. Sung, H.-J. Kim, Thin Solid Films **515**, 4996 (2007)
29. A.S. Hassanien, A.A. Akl, Phys. B Condens Matter **576**, 411718 (2020)

30. F.S. Mahmood, R.D. Gould, A.K. Hassan, H.M. Salih, Thin Solid Films **270**, 376 (1995)
31. F. Khojasteh, M.R. Mersagh, H. Hashemipour, J. Alloys Compd. **890**, 161709 (2022)
32. S.M. Fawzy, G.E. Khedr, N.K. Allam, Int. J. Hydrogen Energy **48**, 33111 (2023)
33. R.S. Dubey, S.R. Jadkar, A.B. Bhorde, ACS Omega **6**, 3470 (2021)
34. M. Boudiar, F. Hanini, A. Bouabellou, Y. Bouachiba, A. Taabouche, D. Dergham, C. Redjeb, J. Sol–Gel Sci. Technol. **107**, 430 (2023)
35. Y. Sari, P.L. Gareso, D. Tahir, Int. J. Environ. Sci. Technol. (2024). https://doi.org/10.1007/s13762-024-05879-z
36. B. Geng, X. Yang, P. Li, W. Shi, D. Pan, L. Shen, ACS Appl. Mater. Interfaces **13**, 45325 (2021)
37. H. Tecimer, T. Tunç, Ş Altındal, J. Mater. Sci. Mater. Electron. **29**, 3790 (2018)
38. Ç. Çetinkaya, J. Mater. Sci. Mater. Electron. **33**, 16597 (2022)
39. E. Erbilen Tanrıkulu, İ Taşçıoğlu, J. Electron. Mater. **52**, 2432 (2023)
40. G. Özel, S. Demirezen, J. Mater. Sci. Mater. Electron. **35**, 946 (2024)
41. C. Bairam, Y. Yalçın, H.İ Efkere, E. Çokduygulular, Ç. Çetinkaya, B. Kınacı, S. Özçelik, Phys. B Condens Matter **616**, 413126 (2021)
42. Y. Yalçın, Ö. Arslan, C. İldeş, E. Çokduygulular, Ç. Çetinkaya, B. Kınacı, J. Mater. Sci. Mater. Electron. **34**, 1 (2023)
43. B. Kinaci, S. Özçelik, J. Electron. Mater. **42**, 1108 (2013)
44. J.R. Brews, E.H. Nicollian, Solid State Electron. **27**, 963 (1984)
45. S.M. Sze, *Semiconductor devices: physics and technology* (John Wiley & sons, 2008)
46. Ç.Ş Güçlü, M. Ulusoy, Ş Altındal, J. Mater. Sci. Mater. Electron. **35**, 881 (2024)
47. E.H. Rhoderick, R.H. Williams, *Metal-semiconductor contacts* (Clarendon press, Oxford, 1988)
48. N. Delen, S.A. Yerişkin, A. Özbay, İ Taşçıoğlu, Phys. B Condens Matter **665**, 415031 (2023)
49. G.H. Thomas, A.A. Kumar, V.R. Reddy, V. Janardhanam, C.-J. Choi, Mater. Today Proc. **9**, 26 (2023)
50. S. Demirezen, A. Arslan Alsaç, H.G. Çetinkaya, Ş Altındal, J. Mater. Sci. Mater. Electron. **34**, 1186 (2023)
51. H.U. Tecimer, M.A. Alper, H. Tecimer, S.O. Tan, Ş Altındal, Polym. Bull. **75**, 4257 (2018)

Publisher's Note Springer Nature remains neutral with regard to jurisdictional claims in published maps and institutional affiliations.

Springer Nature or its licensor (e.g. a society or other partner) holds exclusive rights to this article under a publishing agreement with the author(s) or other rightsholder(s); author self-archiving of the accepted manuscript version of this article is solely governed by the terms of such publishing agreement and applicable law.